The electron temperature of the inner halo of the Planetary Nebula NGC 6543

S. Hyung[1], G. Mellema[2], S.-J. Lee[3], and H. Kim[4]

[1] Korea Astronomy Observatory, 61-1 Whaam-dong, Yusong-gu, Taejon 305-348, Korea
   e-mail: hyung@kao.re.kr
[2] Sterrewacht Leiden, PO Box 9513, 2300 RA, Leiden, The Netherlands
   e-mail: mellema@strw.leidenuniv.nl
[3] Dept. of Astronomy and Space Science, Chungnam National University, 220 Kung-dong, Yusong-gu,
   Taejon 305-764, Korea
   e-mail: seong@canopus.chungnam.ac.kr
[4] Dept. of Earth Science Education, Korea National University of Education, Chung-Buk 363-791, Korea
   e-mail: vitkim@kao.re.kr

Abstract. We investigate the electron temperature of the inner halo and nebular core regions of NGC 6543, using archival Hubble Space Telescope (*HST*) Wide Field Planetary Camera 2 (*WFPC2*) images taken through narrow band [O III] filters. Balick et al. (2001) showed that the inner halo consists of a number of spherical shells. We find the temperature of this inner halo to be much higher (~15 000 K) than that of the bright core nebula (~8500 K). Photo-ionization models indicate that hardening of the UV radiation from the central star cannot be the main source of the higher temperature in the halo region. Using a radiation hydrodynamic simulation, we show that mass loss and velocity variations in the AGB wind can explain the observed shells, as well as the higher electron temperature.

Key words. hydrodynamics – stars: AGB and post-AGB – stars: winds, outflows – ISM: kinematics and dynamics – planetary nebulae: individual: NGC 6543

1. Introduction

NGC 6543 (PN G096.4+29.9) is one of the more intriguing Planetary Nebulae (PNe) because of its complex morphology. The core nebula (the "Cat's Eye") consists of several shells and rings projected on top of each other. Images taken with the *Chandra* X-ray telescope have for the first time revealed the central wind-driven bubble (Chu et al. 2001). Along the symmetry axis, the PN shows FLIERs (Fast Low Ionization Emission Regions).

The object is surrounded by a "giant halo" of 50′, which has an overall spherical morphology, but which at the outer edge consists of many irregularly shaped gas clouds (Middlemass et al. 1989, henceforth MCW89). This giant halo has a low expansion velocity of at most 5 km s^{-1}, and despite its chaotic appearance, it does not show any distinct kinematic features (Bryce et al. 1992). One of the brighter filaments is characterized by a high electron temperature of 15 000 K, derived from an analysis of the [O III] line ratio (MCW89), but by a much

lower temperature of 9000 K when considering the Hα and [N II] 6584 Å profiles (Meaburn et al. 1991).

Recently, Balick et al. (2001) (henceforth BWH01) analyzed archival Hubble Space Telescope (*HST*) images and found that the region just outside the bright core shows at least nine circular "rings", which are in fact projected spherical shells. We will refer to this region as the "inner halo" region to distinguish it from the "outer halo" studied by MCW89 and Meaburn et al. (1991). This inner halo looks much more continuous and regular than the outer halo. Rings like the ones seen around NGC 6543 are quite common, and are found around AGB stars like IRC 10216 (Mauron & Huggins 2000), post-AGB stars like CRL 2688 (Sahai et al. 1998), and other PNe, such as NGC 7027, and Hb 5. The time scale associated with the implied mass loss variations are typically 100–1000 years, which is too long to associate them with the pulsations of AGB stars, and too short to connect them to thermal pulses. They could originate from variations inherent to the nature of the mass loss mechanism during the AGB phase (Simis et al. 2001), or from stellar magnetic field variations (Soker 2000; Garcia-Segura et al. 2001), or from

Table 1. *WFPC2* archive images.

Name	Filter	[Ion] line	Exp Time (s)
U27Q0103T	F437N	[O III] 4363	1200
U27Q010AT	F502N	[O III] 5007	600
U27Q010FT	F656N	Hα	200

All these observations were performed on September 18, 1994.

the influence of a companion star (Harpaz et al. 1997; Mastrodemos & Morris 1999).

The central star of NGC 6543 is a Wolf-Rayet star of spectral type [WC 8]. The P Cygni profiles of, for example, C IV and N IV in its spectrum indicate a terminal wind velocity of $V(\infty) = 2150$ km s^{-1} (Castor et al. 1981). The chemical abundances in NGC 6543 are likely to be position dependent (Hyung et al. 2000). Its distance is not well known; values derived through statistical methods are around 1 kpc, and according to other methods it could be as close as 500 pc. We will assume a distance of 1 kpc.

In this paper, we investigate the inner halo region by deriving the [O III] 5007/4363 line ratio from archival narrow band *HST* images, using a proper interstellar extinction correction. This procedure and the results are described in Sect. 2. In Sect. 3 we attempt to explain the results using both photo-ionization and radiation-hydrodynamic modelling. We discuss the results in Sect. 4, and summarize our conclusions in Sect. 5.

2. HST/WFPC2 data

The *HST* archive images are available from the *HST* archival data centre. The [O III] 4363 and 5007 emission-line images can be used to find an [O III] electron temperature map. We searched the archive for *WFPC2* images of [O III] and Hα/Hβ. As will be explained below, we need an Hα or Hβ image to eliminate the continuum contribution from the [O III] images. The *HST* archive contains 11 images of NGC 6543 in these filters. After careful examination, we selected the three best ones: U27Q0103T ([O III] 4363); U27Q010FT (Hα); and U27Q010AT ([O III] 5007). The central part of the [O III] 4363 image is saturated by the central star. See Table 1 for the details.

2.1. Reduction of the WFPC2 images

The archived *WFPC2* images have already been calibrated via the pipeline procedure, i.e. the analog-to-digital correction, bias level removal, bias image subtraction, dark image subtraction, flat-field multiplication, and shutter shading correction. Using standard IRAF routines, we removed the cosmic rays. The retrieved images were converted into flux units (or magnitudes) using the header information.

Table 2. *WFPC2* narrow band filter set.

Name (Ion)	Width (Å)	Peak (λ)[1]	Q(20 Å)[2]
F437N([O III])	25.2	49.6 (4368)	86.4%
F502N([O III])	26.9	57.9 (5009)	105.0%
F656N(Hα)	21.9	86.2 (6561)	112.3%

[1]Peak transmission efficiency in % (wavelength λ at peak).
[2]The transmitted light relative to an ideal 20 Å bandwidth filter, assuming this ideal filter has 100% transmission over a with 20 Å bandwidth.

2.1.1. Filter bandwidth correction

The width and transmission efficiency of the three filters differ (see Table 2). To compare the images, one must correct for these differences. We use a normalizing function to obtain the observed photon flux within a bandwidth of 20 Å:

$$F_{\mathrm{norm}} = F_{\mathrm{HST}}/Q(20 \text{ Å}), \qquad (1)$$

where F_{HST} is the calibrated final flux; $Q(20 \text{ Å})$ (given in the last column of Table 2) is the transmission efficiency for an ideal 20 Å bandwidth filter with 100% transmission. Once F_{norm} has been obtained for each image, we may compare them with each other.

2.1.2. Interstellar extinction

The interstellar extinction is corrected using the relation

$$F_{\mathrm{e-c}} = F_{\mathrm{norm}} \times 10^{C \cdot k_\lambda}, \qquad (2)$$

where C is the logarithmic extinction coefficient at Hβ, and k_λ the extinction parameter from Seaton (1979). $C(\mathrm{H}\beta)$ values of 0.18, 0.20 and 0.30 have been presented by Kaler (1976), Middlemass et al. (1989), and Hyung et al. (2000), respectively. In what follows we will adopt $C(\mathrm{H}\beta) = 0.20$. The uncertainty in the adopted C value does not affect the results derived in this paper.

2.1.3. Continuum correction

The filter widths are ∼20 Å, while the full width at half maximum ($FWHM$) of the emission lines is only ∼1 Å. Thus, the images can contain a significant contribution from continuum photons. Since no offset nebular filter images are available in the *HST* archive, and the continuum is mostly produced by hydrogen quanta (see below), we used the Hα *WFPC2* image to correct for the continuum contribution in the [O III] filter images.

First, we estimated the contribution to the continuum of H recombination plus bremsstrahlung, assuming an electron temperature of 10 000 K and He/H abundance ratios of $N(\mathrm{He}^+)/N(\mathrm{H}^+) = 0.1$ and $N(\mathrm{He}^{++})/N(\mathrm{H}^+) = 0.01$. We find this contribution to be 92.7% near [O III] 4363 emission line, and 91.2% near [O III] 5007. The theoretical continuum-emission coefficients have been
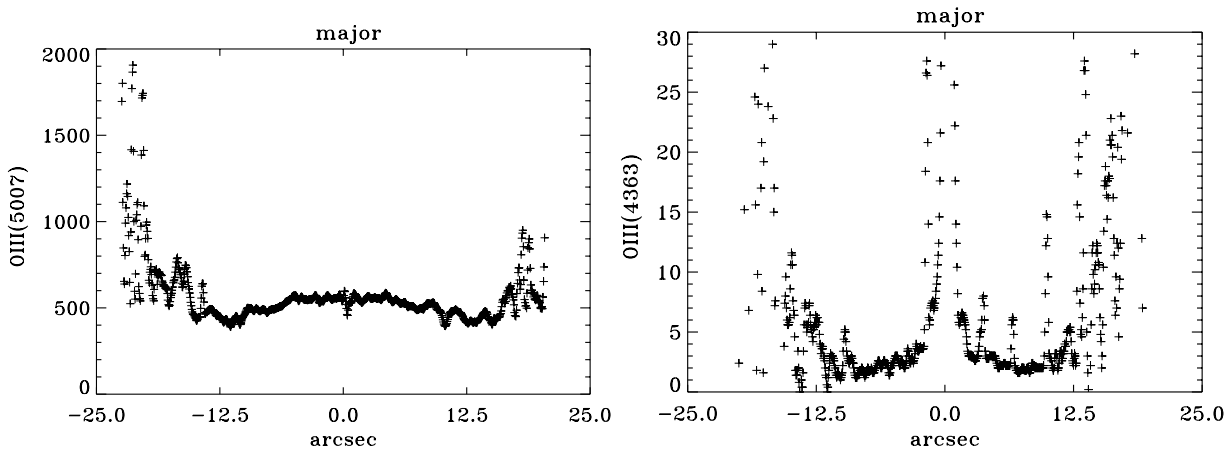
Fig. 1. [O III] intensities along the major axis [scaled to $I(H\beta) = 100$]. On the left $I([\text{O III}]\ 5007)$, on the right $I([\text{O III}]\ 4363)$.

adopted from Brown & Mathews (1970); see their Tables 1–5. This simple calculation shows that hydrogen emission dominates the continuum at the wavelengths of interest.

The continuum-corrected [O III] images can then be obtained from the following relations,

$$F_f(5007) = F_{e-c}(5007) - F_{e-c}(H\alpha) \times A(5007), \quad (3)$$

$$F_f(4363) = F_{e-c}(4363) - F_{e-c}(H\alpha) \times B(4363), \quad (4)$$

where $A(5007)$ and $B(4363)$ are the extinction-corrected continuum fluxes near 5007 Å and 4363 Å, respectively, divided by the extinction-corrected continuum flux near the Hα line + the Hα emission flux itself. Values for A and B were derived from our ground-based Hamilton Echelle Spectrograph (*HES*) data (Hyung et al. 2000): $A(5007) \simeq 1.21 \times 10^{-3}$ and $B(4363) \simeq 5.28 \times 10^{-3}$. Aller (1984) lists the theoretical values as $A(5007) = 3.1 \sim 4.4 \times 10^{-3}$ and $B(4363) = 3.5 \sim 6.2 \times 10^{-3}$, and also shows that $B(4363)/A(5007) \sim 1.2$. Our B value agrees with this within 20%, but we find a 3 to 4 times smaller value for $A(5007)$. This deviation is probably caused by an overcorrection for scattered light in analysis of the *HES* data. As a test we also derived the values for the bright core nebula, and there our procedure does reproduce the expected theoretical values. However, the strength of the [O III] 5007 is such that an error of a factor of four in $A(5007)$, only affects the derived intensity to less than 0.5%. An error of about 20% in $B(4363)$ also does not influence our results.

Although the ratio of continuum to line emission may have positional variations, we assume that A and B remain constant throughout the nebula and halo. This assumption is unavoidable, due to the unavailability of offset continuum filter images. It may be not a bad assumption, since the stratification effect of the Hα (or Hβ) recombination image is generally not conspicuous, compared with that of the line images, e.g. [O III] 5007 or [N II] 6548. The F437N image may suffer from some light contamination by Hγ at 4341 Å.

Table 3. [O III] line intensities.

Name (Ions)	Core (North)[1]	Core (East)[1]	Halo[2]
[O III] 4363	2.05	1.58	28
[O III] 5007	704	518	1528

[1]Hyung et al. (2000).
[2]MCW89.
Note: Extinction corrected intensities are given based on $I(H\beta\ 4861) = 100$ ($C = 0.2, 0.3$ for *HST* and *HES*, respectively). See the main text.

In order to reduce the scatter, we rebinned the image from $0\rlap{.}''1 \times 0\rlap{.}''1$ to $0\rlap{.}''3 \times 0\rlap{.}''3$ pixels. Figure 1 displays the [O III] 5007 and 4363 line intensities on a flux scale where $I(H\beta) = 100$. Note how the [O III] 4363 intensities within $\sim 2''$ of the centre are strongly affected by the saturation caused by the central star.

Table 3 lists the spectroscopic line intensities of the core H II region (Hyung et al. 2000) and the outer halo (MCW89). A comparison with Fig. 1 shows that, within the uncertainties, the correspondence between the spectroscopic data and the images is reasonable.

2.1.4. [O III] temperature map

Figure 2 shows the temperature maps for three different electron temperatures ranges: $T_e = 8000 - 9000$ K; $11\,000 - 12\,000$ K; and $13\,000 - 14\,000$ K, respectively. As was found in previous ground-based studies, the electron temperature of the core nebula is 8000–9000 K. The $11\,000 - 12\,000$ K image clearly displays an ellipsoidal envelope surrounding the core nebula. Figure 2c shows that the inner halo region contains hotter material of $T_e \sim 14\,000$ K. The temperature in the very central region also appears to be high. However, those values are suspect, due to the saturation by the central star in the [O III] 4363 image.

In Fig. 3, we plot the electron temperature distribution along the major and minor axes, and at an intermediate

angle. The position angles are $-32°$, $+58°$, and $+13°$, respectively.

We estimated the errors in Figs. 2 and 3 using a qualitative analysis. We found them to be less than $\triangle T_e \sim$ 500 K in the core nebula, and at least three times larger in the inner halo, $\simeq 1500$ K. This latter region could be partly filled with relatively low temperature gas, like that seen in Fig. 2a. In this case, the scatter in Fig. 3 may reflect real temperature fluctuations involving geometrical irregularities. Otherwise, it would be due to errors of around 3000 K in the halo.

Figure 3 shows a number of local peaks with $FWHM \sim 0.''3-0.''4$, where the electron temperature increases sharply. These could be due to blobs or filaments. We compared temperature profiles, e.g. $0.''8$ apart, parallel to the major and minor axes. No structure survived in the next adjacent scan; apparently, blobs substantially larger than $0.''4$ do not exist. This leads to the conclusion that any existing substructures must be about $0.''4$ (0.002 pc for an assumed distance of 1 kpc), or less.

Figure 3 also shows third order Legendre polynomial curves fitted to the radial electron temperature distribution (excluding the central region). These fits suggest that the maximum electron temperature in the halo occurs at a radial distance of $r \sim 0.09$ pc ($18''$, $17''$, and $14''$, respectively), beyond which it falls off again. The radial distribution of the *HST* electron temperature suggested by the polynomial fitting indicates a high electron temperature location, which may roughly form a complete circle of $r \sim$ 0.09 pc. The halo temperature fitting found from the *HST* images may be the projection of a relatively large shell, of $r \sim 0.09-0.1$ pc.

3. Excitation by hardened UV or shock?

The thermal properties of the gas in the halo are set by photo-ionization heating, and also possibly by shock heating. We will now investigate whether these two processes can explain the observed electron temperatures.

3.1. Hardening of the UV radiation field

Long ago, Aller et al. (1939) suggested that a hardening of the UV radiation field from the central star might be responsible for a rise of T_e in the outer part of photoionized PNe. Photoionization modeling by Hyung et al. (2000) suggested that the electron temperature near the outer boundary (at 0.056 pc) of the core H II region of NGC 6543 is higher than that of the inner region (at 0.05 pc) by 600 K, due to a hardening of far UV stellar radiation. Can this hardened stellar UV radiation also raise the electron temperature of the halo gas to the value suggested by the *HST* [O III] images? MCW89 showed that the emission in the outer halo could not be produced by photo-electric heating: they were only able to reproduce a halo temperature some 2000 K above the core region temperature.

We extend the photoionization model by Hyung et al. (2000) to see whether the hardened UV radiation from the WR-type central star produces the high electron temperatures in the inner halo, or gives the observed [O III] 5007/4363 line ratios. Note that the photoionization model by Hyung et al. (2000) indicates that NGC 6543's bright core is density bounded. Thus, there are still plenty of hard, far-UV photons available to ionize the gas in the halo region. Since the relatively low density (35 cm^{-3}) outer halo case was already tested by MCW89, we explore higher densities for the inner halo gas. The description of the photoionization model, the improved Sobolev approximation (ISA) model atmosphere for the hydrogen deficient Wolf Rayet type central star of the planetary nebula (CSPN), and references to selected atomic parameters may be found in Hyung et al. (2000). We adopted the abundances from the core nebula, as described by Hyung et al. (2000). The results show that a higher electron temperature can only be achieved for very high densities. For, example, the model with $N_H = 10^5$ cm^{-3} and a small filling factor, $f = 0.0001$, gives $I(4959+5007)/I(4363) =$ 105.8 (corresponding to $T_e \sim 12\,000$ K). Since the spectroscopic observations indicate that the electron density in the halo is low, this high density model is not an appropriate solution to the halo emission. Nonetheless, there may be some implications for the physical conditions of the filaments observed in the central or halo region of some PNe – the filaments are density enhanced structures, in any case.

3.2. Shock heating

An alternative way to heat gas is through shocks. Shocks are caused either by pressure or velocity differences. In order to produce a noticeable temperature increase of the order of 15 000 K, the shock speed needs to be at least 20 km s^{-1}. One origin for such shocks would be a "leaky" stellar wind bubble. If the material which the fast wind is running into is quite clumpy, a mass-loaded flow would proceed beyond the core nebula into the halo region, where it would interact with halo material to produce the necessary shocks. This is the model favoured by Meaburn et al. (1991) to explain the measured electron temperatures in the outer halo. Whereas the structures in the outer halo also morphologically suggest such an interaction, the inner halo looks much smoother, and shows no signs of interacting with a mass-loaded flow from the core. In fact, with the parameters given in Meaburn et al. (1991), the density in the inner halo would be dominated by the mass-loaded flow. In support of the mass-loaded flow model, we should mention that the images presented in BWH01 do reveal radial structures in the inner halo, which mostly (but not uniquely) appear to originate from the FLIER regions in the core nebula. If these are extensions of a faster outflow in the FLIERs, and not illumination effects, they could certainly produce (local) shocks in the inner halo.
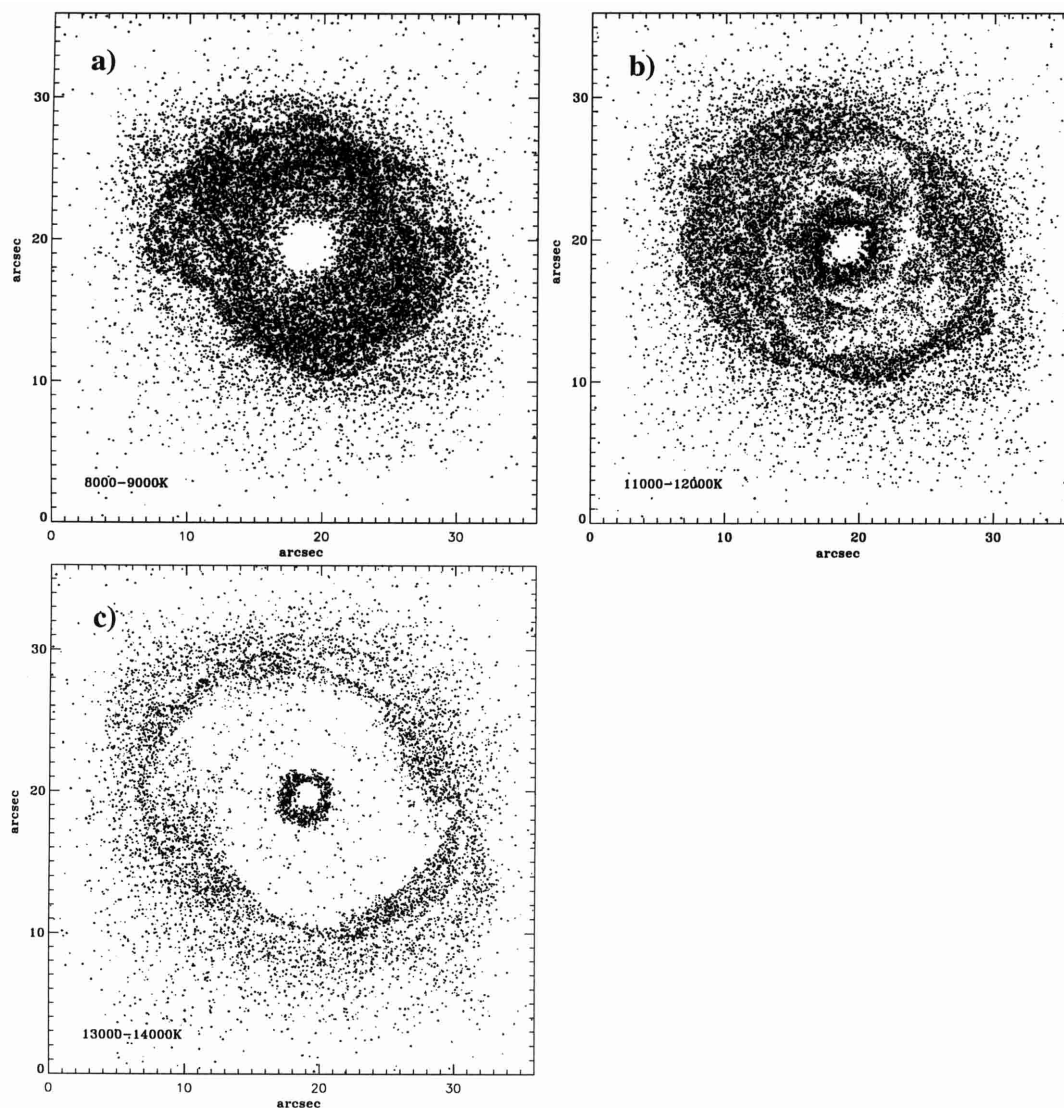
Fig. 2. [O III] temperature maps for the ranges **a)** $T_e([\text{O III}]) = 8000 \sim 9000$ K, **b)** $T_e([\text{O III}])$ $11\,000 \sim 12\,000$ K, **c)** $T_e([\text{O III}])$ $13\,000 \sim 14\,000$ K. An upper limit of $20\,000$ K has been set for the area around the CSPN.

On the other hand, the presence of the rings in the inner halo region already indicates that there are density and hence pressure differences there. The idea that the inner halo is dynamic is strengthened by the increase in the line widths in the inner halo region to about 30 km s^{-1} (Bryce et al. 1992; BWH01), which could be explained by a superposition of faster moving shells. In this case the shells would have velocities well in excess of the 5 km s^{-1} derived for the outer halo. If the shells were created while the CSPN was on the AGB, velocity differences would also have helped in their survival up to the current era. Density variations without velocity variations tend to be smoothed out. If the shells are produced by the mechanism explained in Simis et al. (2001), velocity differences of 50 km s^{-1} or higher can be reached (Simis, private communication).

It will be difficult to measure the true expansion velocity of the shells, since the slit position which would capture

it the best, would also contain the bright and kinematically complicated core nebula (see Miranda & Solf 1992).

3.2.1. Numerical model

In order to show the feasibility of shock heating by the shells, we set up a simple numerical experiment. For this we use a hydrodynamic code coupled to a photo-ionization calculation. The hydrodynamic part of the code is based on Roe's approximate Riemann solver (Mellema 1993; Eulderink & Mellema 1995). In each numerical time step, the heating and cooling rates are calculated using the *DORIC* routines (Raga et al. 1997; Mellema et al. 1998), which calculate the non-equilibrium ionization, heating and cooling of the gas. Since we are not concerned with the shaping of the entire nebula, and want to resolve the post-shock cooling region, we consider only the one-dimensional (spherical) case. For this we used $12\,000$ computational
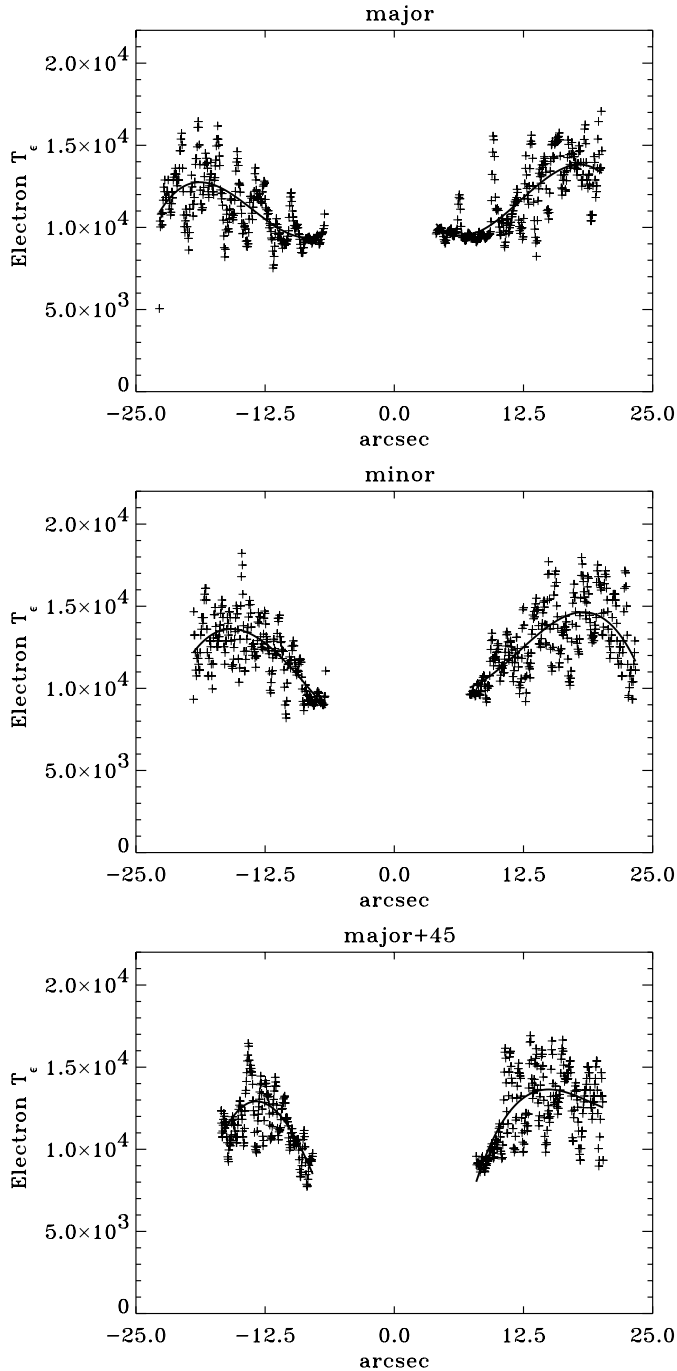
Fig. 3. [O III] electron temperatures in K: from top to bottom: along the major axis, along the minor axis, and in between the major and minor axes (at major +45°). Since binning of 3×3 pixels was applied, the spatial resolution is $0\rlap{.}''3$. We exclude the region near the CSPN.

Table 4. Input parameters for the simulation.

$\dot{M}_{\mathrm{low}}$	4×10^{-6} $M_\odot$ yr^{-1}
v_{low}	40 km s^{-1}
$\dot{M}_{\mathrm{high}}$	2×10^{-5} $M_\odot$ yr^{-1}
v_{high}	80 km s^{-1}
$\tau_{\mathrm{variation}}$	200 years
r_{in} (boundary)	0.05 pc ($10''$)
r_{out} (boundary)	0.15 pc ($30''$)
Δr	6.48 μpc
Central Star T_{eff}	48 000 K
Central Star L	3510 $L_\odot$

Thus, we set the inner radius of the computational grid to be 0.05 pc, and let the grid run out to 0.15 pc.

At the start of a simulation, the value of the electron temperature is given by the equilibrium temperature provided by the photo-ionization model.

For the abundances, we used the values derived by Hyung et al. (2000) for the core nebula: He/H = 0.13, C/H = 5.0 (−5), N/H = 1.2 (−4), O/H = 3.0 (−4), Ne/H = 5.0 (−5), S/H = 7.0 (−6).

Bryce et al. (1992) found the outer halo to be kinematically inert, with an upper limit to the expansion velocity of 4.6 km s^{-1}. The observed electron density of the halo region obtained from the [O II] diagnostics can set a constraint for the mass loss rate of the slow wind. Middlemass found 35^{100}_{-35} cm^{-3} (in the outer halo, outside the *HST* image). Taking a (pre-shock) number density of $n_{\mathrm{H}} \sim 20$ cm^{-3} at 0.15 pc, we arrive at a mass loss rate for the slow wind of $\dot{M}_{\mathrm{slow}} = 10^{-6}$ $M_\odot$ yr^{-1}. Alternatively, BWH01 find a total mass of $\sim$0.1 $M_\odot$ ejected between 17 500 and 6500 years ago (assuming a slow wind velocity of 10 km s^{-1}), which gives a mass loss rate of $\sim$10^{-5} $M_\odot$ yr^{-1}. For a slower wind velocity of 5 km s^{-1}, one obtains half this value. We take a base slow wind mass loss rate of 10^{-6} $M_\odot$ yr^{-1}.

At the inner edge of the grid, we then vary the mass loss rate between this base value and 10^{-5} $M_\odot$ yr^{-1}, and with a velocity difference of 40 km s^{-1}. The variation is sinusoidal with a period of 200 years.

The typical sound speed in an ionized gas is around 10 km s^{-1}. This means that if we choose a base inflow velocity of 5 or 10 km s^{-1}, the inflow will be close to sonic. In this case a steady wind will quickly accelerate (similar to a Parker wind solution) and achieve supersonic velocities. In practice this means that a fixed inner boundary inflow velocity of around 10 km s^{-1} cannot be used. In previous simulations (see e.g. Mellema 1994), this was never a problem, since the inflow velocity was the highly supersonic fast wind. Here, where we want to concentrate on the halo, this physical behaviour poses a problem. To get around this, we decided to use inflow velocities which are well over sonic. In practice this means a base inflow velocity of 40 km s^{-1}, and consequently a peak inflow velocity of 80 km s^{-1}. We scaled the mass loss rates up by a factor of 4 and 2, to achieve roughly the same densities as before.
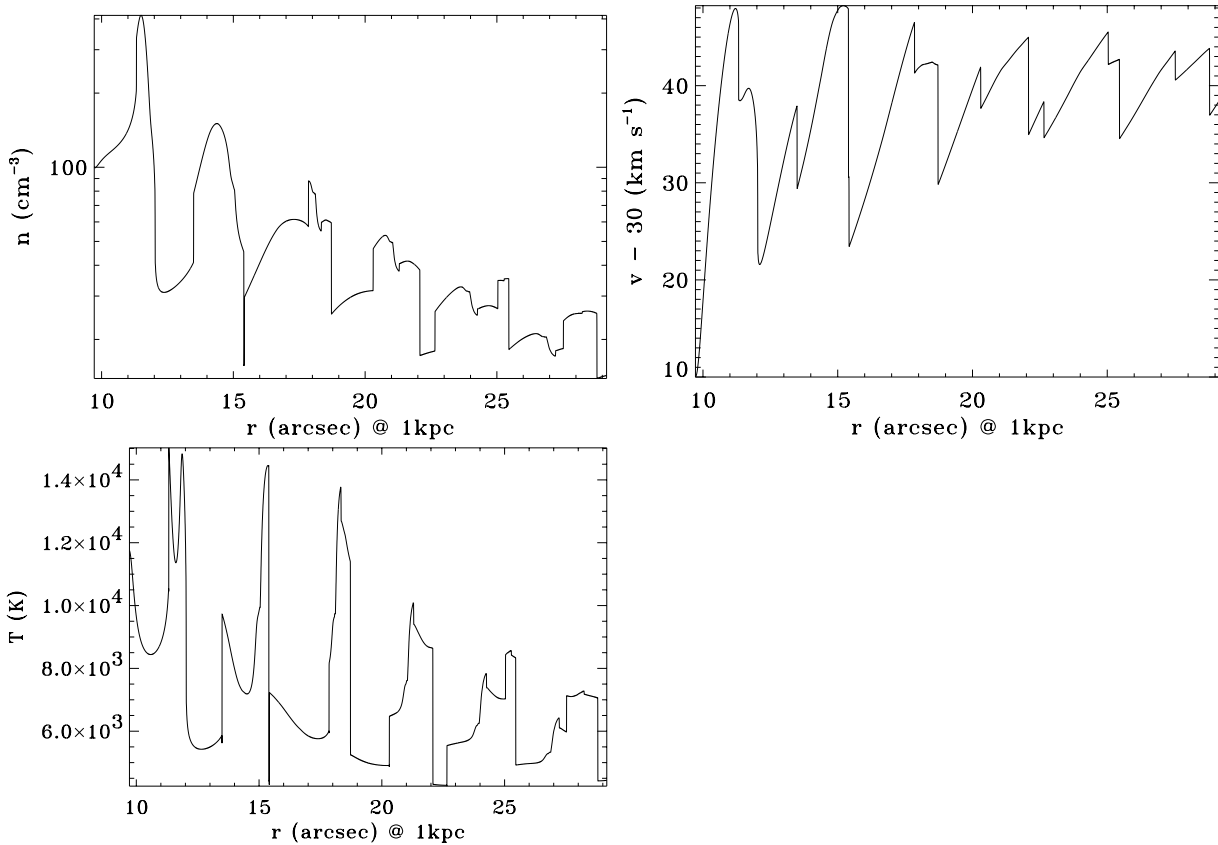
cells of size 2×10^{11} cm. At this cell size, the Courant-Friedrichs-Lewis (CFL) time step imposed by the hydrodynamics is much smaller than the cooling time, and all cooling regions are well resolved.

The optical radius of the main core is about $10''$, while the halo region shown in the *HST* images corresponds to an area with a radius of about $30''$, which is 0.15 pc.

Fig. 4. Hydrodynamics simulation. Graphs showing the number density (n), velocity (v), and temperature (T). The time is 2550 years.

For the photo-ionization calculation we assumed the column densities at the inner grid edge to be 10^{12} cm^{-2} for H I and He I, and 10^{15} cm^{-2} for He II. The parameters adopted in the simulation are listed in Table 4.

3.2.2. Results of the simulation

Figure 4 shows plots of the density, velocity and temperature at 2550 years after the start of the simulation. The situation shown is the periodic solution which develops after roughly 1200 years. One sees the result of a series of pulses, which are interacting and moving out. One should realise that the faster parts of a pulse will run ahead of the slower ones, and may be overtaken by the next pulse, leading to complicated structures as a function of distance. The velocity shows a "saw-tooth" profile, which is still slightly accelerating outward.

Since our hydrodynamic model includes a photoionization model, we are able to construct the $I(5007)/I(4363)$ ratio from the local electron density, temperature, and O^{2+} density. We calculated the emission, turned it into a three-dimensional distribution and projected this on the sky. In Fig. 5 we show the [O III] 5007+4959 intensity, both as function of radius, and along a radial cut through the image. One sees that the image shows the

typical emission characteristics of projected shells, just as seen in the observations, cf. BWH01.

Figure 5 also shows the electron temperature derived from the $I(5007+4959)/I(4363)$ ratio in the projected images, as well as on a cut through a projected temperature map weighted with the H recombination emission. All image data were smoothed with a Gaussian of $FWHM$ of $0.''3$. The synthesized data can reproduce the electron temperatures found in the HST results, including the drop in temperature as function of radius. The projection actually tends to hide the biggest variations in the line ratio, which is due to the small filling factor of the areas of the highest temperature. Comparing the cuts through the two temperature maps, one can see how the [O III] ratio does give higher temperatures, as seen in the case of the so-called "temperature fluctuations". Note also how there actually is a slight displacement between the high temperature peaks in both images. This is because the H recombination-weighted image has a much stronger bias for areas of higher density.

In Fig. 6, we illustrate the effect of the velocity variations by showing synthesized line shapes at four different positions. The velocities from the simulation were decreased by 30 km s^{-1}, and then smoothed both along the velocity ($FWHM$ 10 km s^{-1}) and positional ($2''$) directions in order to simulate the groundbased observations.
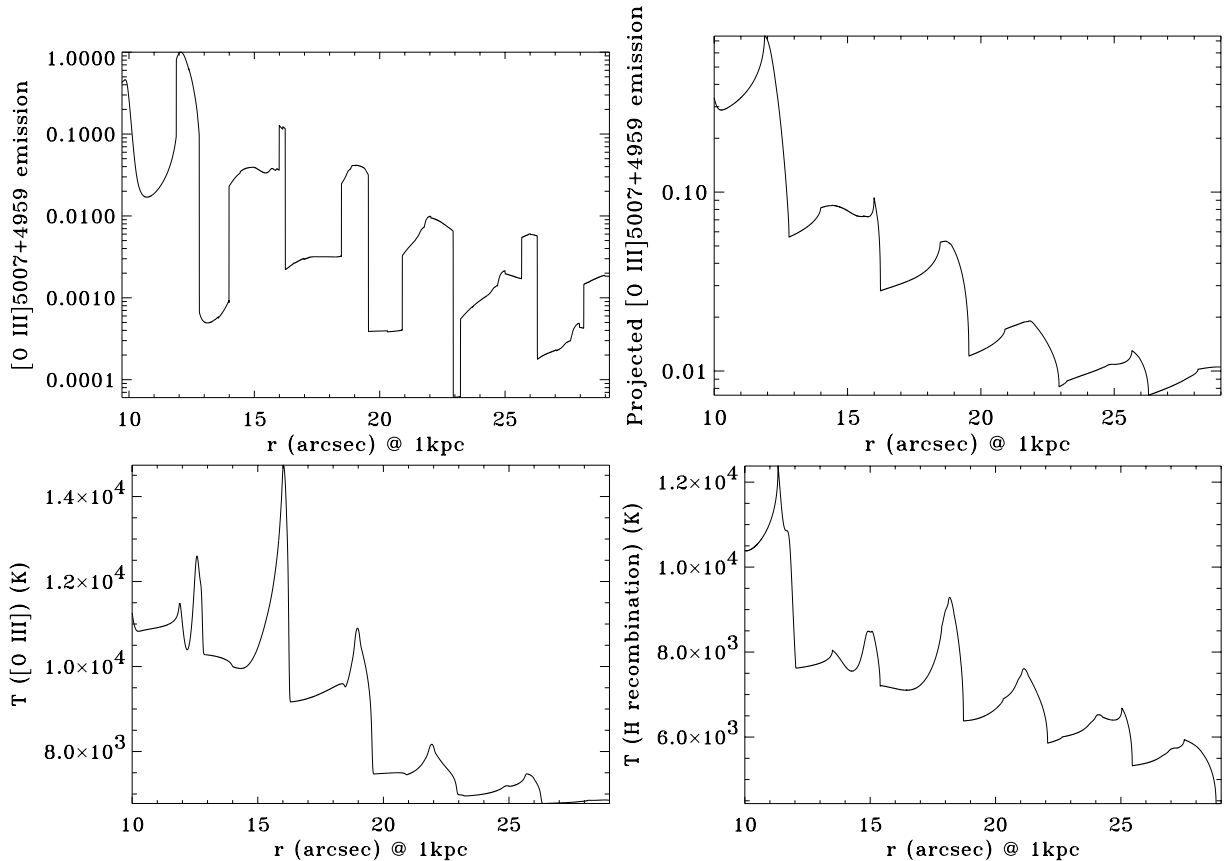
Fig. 5. Top left: [O III] (5007+4959) intensity as a function of radius, in arbitrary units. Top right: the same but projected on the sky. Bottom left: the electron temperature derived from the [O III] (5007+4959)/4363. Bottom right: the electron temperature derived from H recombination; also compare these temperatures to those in Fig. 4.

One sees how, at all four positions, the profiles are quite wide, consistent with the observations. However, they are not Gaussian; the fact that they orginate from different shells is still visible. Since no line shapes have been published, it is hard to say how far our calculations deviate from the observations.

4. Discussion

The results of the simulation show that the interaction between mass loss variations can reproduce shells which match the observed ones morphologically, and to a large extent also kinematically and thermally. This is the first attempt at modelling properties of the shells, other than their appearance. However, both the observational data and the modelling need improvement, and the results presented here should be viewed as a simple, first attempt model.

To start with the observations, narrowband images are not the best method for measuring line ratios accurately, and a closer look at the kinematic data would not hurt either. It would also be very interesting to see if similar effects are found in other PNe with surrounding rings. Unfortunately, the ideal observations would be difficult to carry out; to resolve the individual shells, one needs the *HST*, but in order to do the spectroscopy on these faint shells one needs a large aperture. Also, the velocity resolution of the *STIS* instrument on board *HST* is insufficient for a proper analysis of the line shapes.

The shortcomings of the numerical model are obvious. For one, we were forced to introduce an unrealistically high inflow velocity, and we set the variations to be sinusoidal, which is hardly what one would expect. Ideally one would like to follow the mass loss variations while the star is still on the AGB, and let the different phases interact among themselves, and then study the effect of photo-ionization when the central star evolves into a post-AGB star. One would also like the mass loss from the star to vary with its properties, so that a faster post-AGB wind starts to interact with the inner parts of the AGB wind. This would solve the problem of the subsonic inflow condition, as well as the question of the column density of the core nebula. In short one would model the evolution of the circumstellar material from the (late) TP-AGB until the PN phase. This has, for example, been done by Steffen & Schönberner (2000), but their results do not address the points raised in this paper. We plan to modify our simulations in order to model mass loss variations during the AGB phase, and also their fate after the star evolves off the AGB.

A further complication is the relation between the inner halo/ring area and both the core nebula and outer halo. Compared to these two structures, the inner halo
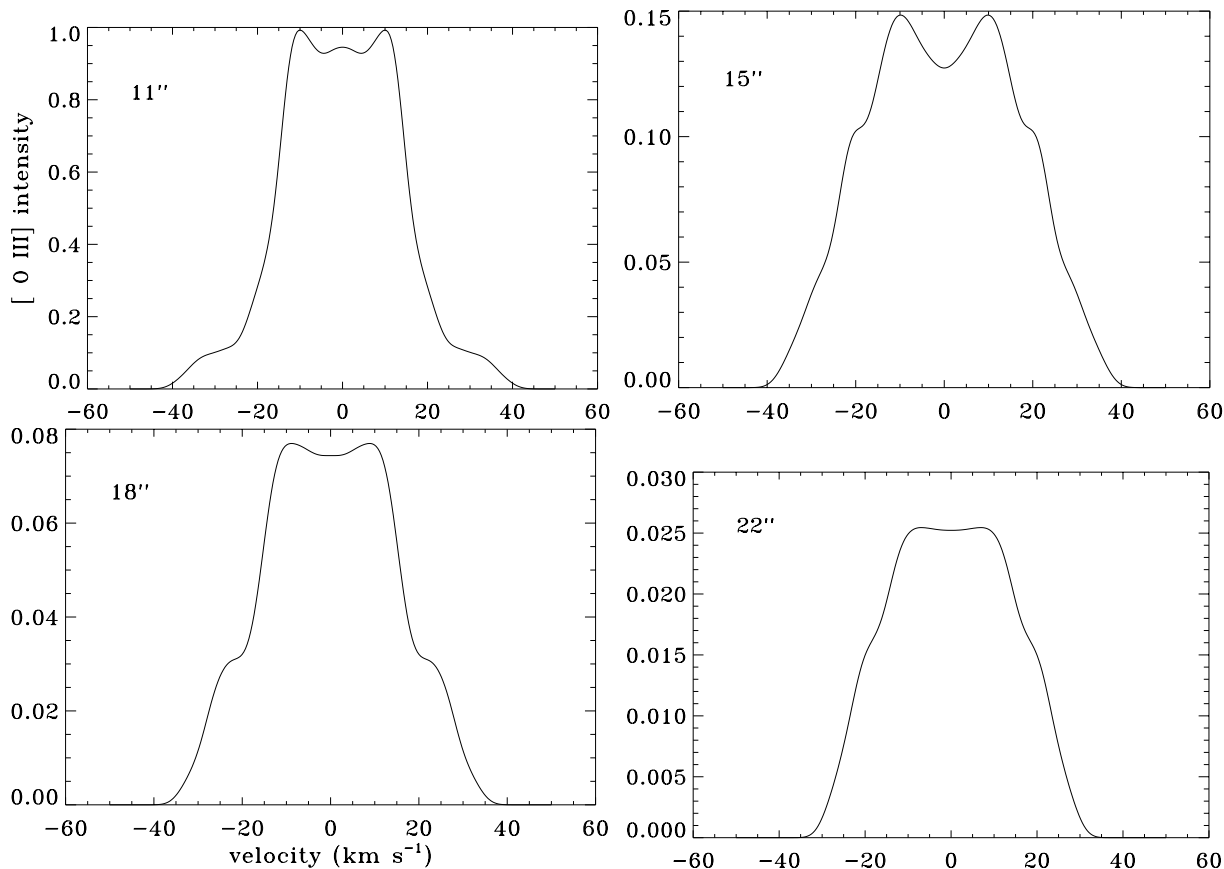
Fig. 6. Line shapes for [O III] 5007 at 11″, 15″, 18″, and 22″ from the central star (for a distance of 1 kpc). The data has been convolved with a Gaussian to achieve 10 km s⁻¹ $FWHM$ velocity resolution, and also 2″ spatial resolution.

seems an oasis of simplicity. The *Chandra* data have shown that the core nebula consists of an inner wind-swept elliptical nebula, surrounded by a (bipolar?) structure of lower ionization, pierced by FLIERs or jets along the major axis. The chaotic structure of the outer halo also points to some dynamic interaction, altough this material was presumably lost long before the inner halo and core nebula. The complete story of NGC 6543 has not yet been finalized.

Still, it may be that the inner halo is indeed a relatively quiet area of material lost just before the star turned off the AGB, in a period in which the mass loss was variable in density and velocity, something which according to some mass loss models is more likely to happen at the higher effective temperatures and luminosities towards the end of the AGB (Simis, private communication). The numerical study presented above shows that such a model can explain the properties of the "rings around the Cat's Eye".

5. Conclusions

We analyze archival *HST* [O III] 4363 and 5007 Å narrow-band images and find an increased inner halo electron temperature of ∼15 000 K for NGC 6543. This higher temperature is found in the same region as the "rings around the Cat's Eye" reported by BWH01. This higher electron temperature cannot be explained by photo-ionization models,

and we conclude that they must be produced by shocks. We show that, in principle, velocity and mass loss variations in the slow AGB wind, required for the production and survival of the rings, would also be able to explain the higher electron temperature in the inner halo, as well as the observed higher velocity dispersion in that region.

References

Aller, L. H. 1984, Physics of Thermal Gaseous Nebulae (Dordrecht: Reidel Publisher), 105
Aller, L. H., Baker, J. G., & Menzel, D. H. 1939, ApJ, 90, 601

Balick, B., Wilson, J., & Hajian, A. R. 2001, AJ, 121, 354 (BWH01)

Brown, R. L., & Mathews, W. G. 1970, ApJ, 160, 939

Bryce, M., Meaburn, J., Walsh, J. R., & Clegg, R. E. S. 1992, MNRAS, 254, 477

Castor, J. I., Lutz, J. H., & Seaton, M. J. 1981, MNRAS, 194, 547

Chu, Y.-H., Guerrero, M. A., Gruendl, R. A., Williams, R. M., & Kaler, J. B. 2001, ApJ, 553, L67

Eulderink, F., & Mellema, G. 1995, A&AS, 110, 587

García-Segura, G., López, J. A., & Franco, J. 2001, preprint [astro-ph/0104154]

Harpaz, A., Rappaport, S., & Soker, N. 1997, ApJ, 487, 809

Hyung, S., Aller, L. H., Feibelman, W. A., Lee, W.-B., & de Koter, A. 2000, MNRAS, 318, 77

Kaler, J. B. 1976, ApJS, 31, 517

Mastrodemos, N., & Morris, M. 1999, ApJ, 523, 357

Mauron, N., & Huggins, P. J. 2000, A&A, 359, 707

Meaburn, J., Nicholson, R., Bryce, M., Dyson, J. E., & Walsh, J. R. 1991, MNRAS, 252, 535

Mellema, G. 1993, Ph.D. Thesis: Numerical models for the formation of aspherical planetary nebulae (Leiden University)

Mellema, G. 1994, A&A, 290, 915

Mellema, G., Raga, A. C., Canto, J., et al. 1998, A&A, 331, 335

Middlemass, D., Clegg, R. E. S., & Walsh, J. R. 1989, MNRAS, 239, 1 (MCW89)

Miranda, L. F., & Solf, J. 1992, A&A, 260, 397

Raga, A. C., Mellema, G., & Lundqvist, P. 1997, ApJS, 109, 517

Sahai, R., Trauger, J. T., Watson, A. M., et al. 1998, ApJ, 493, 301

Seaton, M. J. 1979, MNRAS, 187, 73

Simis, Y. J. W., Icke, V., & Dominik, C. 2001, A&A, 371, 205

Soker, N. 2000, MNRAS, 312, 217

Steffen, M., & Schönberner, D. 2000, A&A, 357, 180